Entangled architecture of rough endoplasmic reticulum (RER) and vacuoles enables topological damping in cytoplasm of an ultra-fast giant cell

1 Ray Chang[†] and Manu Prakash[*,†,‡,¶]

†*Department of Bioengineering, Stanford University, Stanford, CA, 94305*

‡*Woods Institute for the Environment, Stanford University, Stanford, CA, 94305*

¶*Chan Zuckerberg Biohub, San Francisco, CA 94158*

E-mail: manup@stanford.edu

Abstract

Cellular systems are known to exhibit some of the fastest movements in the biological world[1–3] - but little is known as to how single cells can dissipate this energy rapidly and adapt to such large accelerations without sub-cellular damage. To study intracellular adaptations under extreme forces - we investigate *Spirostomum ambiguum* - a giant cell (1-4mm in length) well known to exhibit ultrafast contractions (50% of body length) within 5 msec with a peak acceleration of $15g$.[2,4] Utilizing transmitted electron microscopy (TEM) and confocal imaging, we discover a novel association of rough endoplasmic reticulum (RER) and vacuoles throughout the cell - forming a contiguous fenestrated cubic membrane architecture that topologically entangles these two organelles. A nearly uniform inter-organelle spacing of 60nm is observed between RER and vacuoles, closely packing the entire cell. Using an overdamped molecular dynamics simulation,[5] we demonstrate how this unique entangled metamaterial responds to external loads by rapidly dissipating energy and helps preserve spatial relationships between organelles. Because this dynamics arises primarily from entanglement of two networks incurring jamming transition at a subcritical volume fraction[6] - we term this phenomena "topological damping". Our findings suggest a new mechanical role of RER-vacuolar meshwork as a metamaterial capable of dissipating energy in an ultra-fast contraction event.

High accelerations impart physiological advantages to organisms across all length scales, from speeding cheetahs to the ultra-fast strike of a mantis shrimp.[7,8] In these systems which require repeatable deployment, energy dissipation is critical for the survival of the underlying structures.[9] In movement driven by muscles, active lengthening is observed to specifically dissipate energy, and failure to do so can lead to fractures, torn ligaments, or muscle sprains.[10,11] Specialized structures such as foamy mesocarp layer in durian shell,[9,12] and mineralized helicoidal fibrous structures (telson) near the tail of a mantis shrimp[8] are examples where biological structures protect themselves from damages due to impulse. However, how single cells can resist large forces and dissipate energy in short time scales remains largely unknown. Without cell walls or connective tissues, can a single-celled organism evolve strategies to effectively decelerate and dissipate energy as well?

Spirostomum ambiguum is a giant single-celled organism living in brackish waters, and their extreme contractility is well documented even in early literature.[13] (Figure 1) As a millimeter-scale single-celled ciliate, *Spirostomum* can repetitively contract themselves to less than 50% original body length in less than 10 msec[2] throughout its lifetime. Unlike single-shot ultrafast event such as nematocyst firing[1] which leads to an exploded cell, *Spirostomum ambiguum* demonstrates repeatable contractions via a reversible process of fast contraction and slow relaxation to base state. In our recent studies, we discovered a novel function associated with ultra-fast contractions in *Spirostomum ambiguum* - to enable long range hydrodynamic communication.[4] The ultra-fast kinematics is necessary to break the Stokesian regime and enable long distance wave propagation. The kinematics of this process is composed of a rapid acceleration phase immediately followed by a rapid deceleration, with peak magnitude of both acceleration and deceleration up to $15g$.[4] Previous studies have also measured the peak contraction force to be about 0.6 µN,[14] which is at least 10^4 times greater than the usual forces experienced at cellular level (roughly 10 pN).[15–17] A back-of-the-envelope estimate based on the kinematics of the contraction also predicts a shear rate ($0.2\text{m/s}/(1\text{mm}/2) \sim 400\text{sec}^{-1}$) that is comparable to the wall shear rate in the large artery

of a healthy human.[18] How can *Spirostomum ambiguum* evolve a mechanism to resist such a high force and decelerate effectively?

One unique feature that has been noticed in *Spirostomum ambiguum* for years is their highly vacuolated cytoplasm (also known as vacuolar meshwork, diameter of individual vacuole ranging from 5μm to 30μm) (Figure 1A),[19–21] which is very uncommon except for some other giant single-celled ciliates such as *Bursaria truncatella*, *Homalozoon vermiculare*, and *Loxodes magnus*.[22] In giant phytoplanktons, vacuolation is believed to increase the surface area:cytoplasm ratio and maximize resources acquisition.[23] In mammalian cells and even in protists, cytoplasmic vacuolization is usually associated with various pathological conditions and is often accompanied by cell death.[24–26] However, this is clearly not the case for *Spirostomum ambiguum*, and the biomolecular function of these vacuoles remains poorly understood. By imaging live cells undergoing contraction at high frame rates, we discovered that individual vacuoles deform up to 40% (see Method for estimation of strain) within the cytoplasm akin to a deforming shock-absorbing foam (Figure 1B-C, Supplementary Video S1-S2). Is it possible that the highly vacuolated cytoplasm actually plays a critical role in decelerating the contraction process and participates in energy dissipation?

In order to investigate energy dissipation in this unique cell and identify any damage that might be caused to specific organelles - we map key organelles inside a cell utilizing high resolution imaging such as confocal microscopy and transmission electron microscopy (TEM). Several organelles like the rough endoplasmic reticulum (RER) and mitochondria are distributed across a cell and are good candidates to map. RER particularly, not only forms contiguous networks throughout the cells,[27] but also makes membrane contact sites with other organelles such as mitochondria, Golgi apparatus, lysosomes, peroxisomes, endosomes, and plasma membranes.[28–30] Maintaining the contiguous geometry and membrane contact sites are crucial to their functions in calcium homeostasis, lipid synthesis, lipid exchange, and protein secretion.[28–30]

To understand how ultra-fast cells can protect the organelle architecture and inter-

organelle contact sites while undergoing massive accelerations and deceleration - we decided to map the RER topology with respect to vacuole present in *Spirostomum ambiguum*. To our surprise, we discovered a fenestrated-cubic membrane-like topology of rough endoplasmic reticulum (RER), which is closely wrapping around the vacuolar meshwork. (Figure 2A) Under TEM, the distribution of vacuoles is consistent with our observation in light microscope and early histology studies, with a thin layer of periplasm (2-3 μm) near the cortex enclosing a highly vacuolated endoplasm which spans through the entire organism[19,31,32] (Figure 2B, Supplementary Figure S1). The intimate wrapping relationship we describe here between RER and vacuoles is preserved in both relaxed and contracted organisms(Figure 2A). This unique topology (wrapping) is present throughout the entire cell (Figure 2B). When quantified across the cell - the distance between RER and associated vacuole also has a tight distribution of distance between 30-70 nm in relaxed organism, suggesting sterotypical membrane contact sites (MCS) between these two organelles. In contracted organism, the distance between the RER and its nearby vacuoles have a slightly wider distribution, but it still falls below 150 nm (Figure 2B inset).

Since RER network is contiguous throughout the cell - we also directly observe bridging RER that travel from one vacuole to another nearby vacuole, which is expected for forming a continuous lumen in the cell (Figure 2C). We also find that the RER is fenestrated, with holes puncturing the membrane into many segments. These fenestrated holes provide a conduit between two congruent labyrinths closely tracing around the silhouette of each vacuole. Even when the cytoplasm is invaginated into the vacuoles, the RER still closely follow the outline of the vacuoles (Figure 2D). All the above evidence suggests that there is a linker between RER and vacuoles in *Spirostomum ambiguum*, either through individual proteins or physical forces like electrostatic interactions. Although we cannot clearly identify the mechanism of this linker as yet, we did observe some structures under high magnification which might be associated with proteins between RER and vacuoles (Figure 2E). A more careful structural study is required to identify their identity.

To observe the 3D architecture of the RER-vacuole interaction, we image fixed organisms under confocal microscopy, with the staining of DiOC6(3), an ER marker[33] (Figure 2F, Supplementary Figure S2, Supplementary Video S3-S5). The finding in confocal microscopy confirms our observation under TEM. We clearly see a fenestrated sheet wrapping around the vacuoles throughout the entire cytoplasm. All these observations confirm the presence of a unique metamaterial composed of RER topologically intertwined with the vacuolar meshwork - throughout the cytoplasm (Figure 2G).

Previous studies have shown that highly entangled systems can impart unique mechanical properties, both in the living and nonliving matter. For example, entangled U-shaped particles like staples can stabilize the structure against vibration through inhibition of particle rotation and translation.[34] Living systems like fire ants can also entangle themselves by interlocking their limbs and mandibles, and form waterproof rafts and towers that can be crucial for their survival after floods.[35,36] In polymer rheology, topological characteristics of entanglement, such as linking number and writhe, have been shown to be related to their mechanical properties like storage modulus and loss modulus.[37] Entangled polymer rings, compared to their linear counterparts, also have less shear thinning behavior.[38] In two-phase entangled materials - engineered wire-reinforced granular column have been shown to build freestanding stable structure with high strength under vertical load.[39,40] Recently, interpenetrating lattices have shown enhanced damping properties in 3D printed materials.[41] In simulation of tissues, inclusions can cause marked stiffening of the extracellular matrix, which might explain the compression stiffening of various biological tissues.[42]

Inspired from the geometrical arrangement of RER and vacuolar meshwork, we seek to find if such system can act as a topological damper and control the kinematics of contraction at sub-cellular length scales. In order to understand fundamental link between topological entanglement and it's impact on energy dissipation - we build a 2D entangled hard particle model representation of this unique metamaterial to study its mechanical properties when the system experiences extreme shape changes (Figure 3). In our model, the cell is simplified into

a two-dimensional square, the vacuoles in the cytoplasm are simplified into hard particles, and the RER is simplified into nearly in-extensible strings with zero bending energy. The topological links introduced by the tethered strings mimic the membrane bridges we found under the TEM, which allows us to explore the role of entanglement in the mechanical properties of this unique architecture. Key parameters in our model include the number of particles (N_c), number of strings connecting the particles (N_f), length of the string (l_f), and the relative strength between the repulsive energy among particles and elastic energy of the strings. We also defined filament fraction (ϕ_f) to describe the degree of connectivity or topological constraint in the system, which is defined as the ratio between the number of strings and the number of edges in the Delaunay diagram of the center of the particles (Figure 3A). Volume fraction is defined as the ratio between the total area of particles and the area enclosed by the boundary. We isovolumetrically contract the cell in one axis to 50% of its original length, followed by a very brief holding period and a slow relaxation phase. We imposed a fixed boundary forces and observe the changes in kinematics, and we let the system evolve using an over-damped molecular dynamic scheme. In the study of granular material, 2D models have been shown to be very informative to explore the fundamental mechanisms and are used extensively when new constraints such as particle deformability or surface frictions are introduced.[43,44] Also, we purposefully designed our model to be simple rather than trying to match all aspect of the RER-vacuole system in *Spirostomum ambiguum*, because we believe the topological entanglement we observed suggests a more general design principle to introduce damping function or structural stabilization in a single cell. Detailed descriptions of the model and a list of potential caveats are also summarized in the Method section.

We ran 50 simulations with the same volume fraction of 0.83 (chosen as a sub-critical volume fraction for 2D hard disks) but varying filament fraction (ϕ_f) in order to understand the role of topological entanglement. In this simulation framework, we explore how topological constraints impact the kinematics, boundary forces and energetics of the contraction

process (see Supplementary Video S6-S7 for the simulation videos). In Figure 4, we can see that even though all the simulation starts with a high contraction rate, increasing the degree of topological constraints causes a rapid rise in boundary forces and thus a fast drop in contraction rate, manifesting the role of topological constraints as a "braking" mechanism. We can also see that systems with greater topological constraints encloses larger area in the force-deformation curve, showing that the topological constraints enhances the ability of the system to dissipate energy. Aside from deceleration, preservation of neighboring relationship is also physiologically relevant, as previous studies have demonstrate the importance of organelle connectomes in other eukaryotic organisms.[45,46] By tracing the neighboring relationships among vacuoles before and after a full contraction cycle, we can see that the system with no topological constraints shows a massive rearrangement of neighboring vacuoles which can potentially break the inter-organelle connections, while the systems with high topological constraints can better preserve the spatial relationship among organelles (Figure 4E&F).

From a mechanistic point of view, the phenomenon of topological damping can be explained via induction of a jamming transition below classical critical volume fraction threshold due to entanglement and formation of force chain propagation. It is well-established that, for 2D hard friction-less spherical particles, when the averaged contact number ($\langle z \rangle$) of the particles exceeds 4, the system is jammed because the total number of constraints ($N_{\mathrm{c}}\langle z \rangle/2$) exceeds the total degree of freedom ($2N_{\mathrm{c}}$) of the system (condition of isostaticity).[6] In our current model for topologically induced damping, we explore how increasing the number of interconnecting strings in the system creates additional contacts between strings and particles under contraction, which also impose additional constraints on the particles and make it easier to be in a jammed state. Classically, it is necessary for granular material to maintain force chain in order to support external load.[47] While it is possible for an under-constrained particle to be part of the force chain, depending on the orientation of the forces, they can potentially rearrange themselves and break the force chain, and their

rearrangement will cause the deformation of the cell. On the contrary, if a particle and at least 4 of its neighboring particles are all over-constrained, it is guaranteed that the particle will participate in force chain transmission, and it is impossible for it to rearrange itself due to topological constraints.

Contraction process studied here is distinct from methods used to explore jamming in a classical context via change in volume fraction. In our system with broken symmetry, we define the X-axis as the direction along which the system contracts and we keep the volume fraction constant. Next we compute the probability of guaranteed force chain transmission as $(p(z_{\mathrm{c}} + z_{\mathrm{f}} \geq 4))^5$, where p denotes probability, z_{c} is the contact number of neighboring particles, and z_{f} is the contact number for non-connecting strings. We discovered that the probability of guaranteed force chain transmission has a strong linear correlation with the peak normalized boundary forces in x-direction (which conceptually represents how much external load is being transmitted internally) and even the entire time series of normalized boundary forces in x-direction during contraction phase (Figure 5 A & B, Figure S5), with a slope very close to 1. Even if we ignore the contact from flexible strings and only consider the averaged contact number among particles as in traditional system, we can also see that the topological constraints cause a prolonged jammed state during the contraction process. Note that as the shape deformation in our simulation is isovolumetric, we did not change the volume fraction of the system. The system is jammed at a sub-critical volume fraction due to topological constraints, which prevent the particles from rearrangement and fully utilize the volume available in the system.

To conceptually demonstrate the idea of topological damping and its potential application and build intuition for this phenomena, we also created a table-top 3D model of simplified metamaterial capturing the key aspects of this unique ER-vacuole system with entangled table tennis balls and inextensible fabric (Figure 5 D-F, see Method section for details). The two systems that we tested have the same number of table tennis balls and same amount of fabrics, but one includes fabric cut into stripes and entangled with the table tennis ball, while

the fabric in the other system simply encloses the table tennis balls in a sealed bag. We can see that the system with topological entanglement has a better ability to resist external load (see Supplementary Video S8-S9), and the differences can also be seen more quantitatively using compression testing (Figure 5F, Supplementary Video S10-S11).

Our study suggests that endoplasmic reticulum can have a mechanical role inside a cell by providing geometric constraints on the vacuolar meshwork and inducing jamming transition. Previous studies have shown mechanical roles of several other organelles. For example, the mechanical support and force anchoring provided by cell nucleus has been shown to be critical in apico-basal force generation, which is essential for tissue morphogenesis.[48] Nucleus has also been shown to act as a piston to increase intracellular pressure, drive the formation of lobopodia, and even direct the cell migration path.[49,50] The central vacuole in plant cell has also long been known for its role in mechanical support, and changes in its turgor pressure are responsible for the rapid movement of tactile sensitive plant.[51] Recently, endoplasmic reticulum has been shown to impact the viscosity of cytoplasm, and failure to reorganize ER during mitosis can cause chromosome missegregation.[52] Our study further suggests that endoplasmic reticulum, being the largest organelle in a cell with a complex geometry while still maintaining a continuous lumen,[53] can induce changes of mechanical properties of the cytosol it resides within - not by its own mechanical strength, but instead by creating geometrical constraints on nearby organelles. For this reason, we label this unique entangled architecture as a metamaterial.

From a physicist perspective, our study also points to a new way to induce jamming.[54] In the traditional phase diagram, a granular system can become jammed through cooling, increasing volume fraction, or decreasing external load. In our athermal topologically entangled system, however, the system becomes jammed by increasing external load without changes in volume fraction. We also propose a mechanism to explain the magnitude of this reactive force in a jammed system through force chain propagation. The prediction are independent from our modeling parameters after normalization and can be predicted by the

probability of guaranteed force chains vacuoles participate in. The basic components of our model is similar to the jammed wire-reinforced granular column.[39,40] However, our study is different from those systems, as the purpose of flexible strings in our model is not to confine a free-standing piles into a rigid structure, but instead to convert confined granular materials into an effective dampers with other biologically relevant functions.

From an engineering perspective, it is very interesting to compare the geometry of our system with previously identified structures which are effective in providing braking, shock absorption or mechanical support. Many types of geometries and architectures have been identified as effective energy absorber and have wide applications in aerospace, military, and civil engineering.[9,55] These include layered cylindrical structure,[56] multi-cell tubes,[57] honeycombs,[58] foams,[59] interdigitated structures,[60] auxetic materials,[61] and interpenetrating lattices.[41] Our table top experiment demonstrates the potential of our topologically entangled granular system to be a new class of shock absorbing materials, which still preserve flexibility and permits deformation but can be readily jammed and this provide mechanical strength when experiencing external load and still remain flexible.

Several other cytoplasmic components could also participate in the energy dissipation process described above, including cortical cytoskeleton. Although it is theoretically possible that the sliding between nearby microtubules can contribute to energy dissipation,[62] the cytoskeleton of *Spirostomum* should be considered more as an actuator of the contraction process and source of energy.[63] Prior experiments demonstrate that when Triton-X treated cells (termed "ghosting" which permeabilizes the cell but also destroys the vacuole morphology) experience high calcium concentration, the cell can be destructed by extreme contraction.[64] This clearly suggests that cytoskeleton itself is not enough to provide the necessary damping function. We also expect an entangled soft particle system should behave differently from an entangled hard particle system, but we believe the general conclusions should still be valid between the two systems. Previous studies have shown the concept of isostaticity still applies to soft frictionless particle system,[6] and the vibrational properties of hard and soft spherical

particles are the same as it approach jamming transition.[65] In our context, we believe the deformability brought by soft vacuoles could make the topological constraint even stronger, as deformed particles have greater perimeters and thus should experience more constraints from wrapped strings. In our future work, we will further elucidate the universality of the principles of topological constraints induced jamming in soft particle systems.

In conclusion, we have discovered a unique entangled ER-vacuolar meshwork topology in *Spirostomum ambiguum*, with a fenestrated ER sheet spanning the entire millimeter-scale single-celled organism, wrapping around the vacuoles. Our work provides a new perspective of role of ER geometry as a metamaterial critical for survival of a cell undergoing rapid acceleration/deceleration cycles. Through modeling and table top experiments, we demonstrate that the topological constraints from the entanglement can provide braking/damping function, dissipate energy inside a cell and help preserve the spatial relationship among organelles against extreme motility, by inducing jamming without changes in volume fraction. Our study suggests a new mechanical role of RER, demonstrates a framework for gigantic cells to organize their organelle architecture efficiently and according to their evolutionary need, and points out a general design principle for a new class of shock absorbing materials.

Material and Method

Culture

Spirostomum ambiguum (Sciento catalog #P346 and Ward's Science catalog #470176-728) was cultured in Hummer medium[66] of spring water infused with Timothy hay (Carolina catalog #132385) and boiled wheat grains (Carolina catalog #132425) as previously described.[4] Organisms used in experiments were extracted in the exponential growth phase. The organisms from Sciento (the company has ceased trading in 2021) were used for the transmission electron microscopy, and the organisms from Ward's Science were used for the confocal microscopy.

Live cell imaging and high speed imaging

The live imaging was performed as previously described method.[4] In brief, the organisms were introduced in a rectangular microfluidic chip (length 2.2cm, width 1cm, height 150μm) of glass slides with copper side walls which act as electrodes. A high speed camera (Phantom V1210 camera, 10000fps) mounted to microscope (Nikon ECLIPSE Ti2, 40X DIC objective) and an electrophysiological DC pulse generator (Grass instruments, S88) were synchronized with a micro-controller (Arduino Uno). Pulse voltage and duration were chosen according to previously reported results.[4]

Estimation of strain from live cell imaging

As the contraction of *Spirostomum ambiguum* has a torsional component, which brings vacuoles away from the focal plane, it is very difficult to track enough number of vacuoles before and after each contraction. Also due to the extremely high speed nature of the contraction process, it is hard to perform 3D imaging. We thus estimated the strain of the vacuoles based on the population statistics of the aspect ratio (AR), and not necessarily keeping track of the same vacuoles. Assuming that the deformation of vacuoles originates from a uniaxial compression force, and assuming that the volume of vacuoles is conserved during the contraction process, we can write the strain of the vacuoles in direction parallel and perpendicular to the compressing force as ε_3 and ε_1, respectively. Based on the assumptions, we can also write $\varepsilon_3 < 0$, $\varepsilon_1 > 0$, $\varepsilon_3 + 2\varepsilon_1 = 0$, $\mathrm{AR} = (1 - 1/2\varepsilon_3)/(1 + \varepsilon_3)$. We thus can estimate the magnitude of compression strain by measuring the aspect ratio of the vacuoles before and after the contraction, and calculate it with $\varepsilon_3 = (1 - \mathrm{AR})/(1/2 + \mathrm{AR})$.

Fixing *Spirostomum ambiguum* in relaxed state

On a glass coverslip, mix *Spirostomum ambiguum* with ice-cold 2X PHEM buffer in 1:1 proportion and put in 4℃ immediately for 15 minutes. Gently mix *Spirostomum ambiguum*

in 1X PHEM buffer with ice-cold 4% glutaraldehyde, 8% paraformaldehyde in 1X PHEM buffer again in 1:1 proportion, and put in 4℃ immediately for at least 1 hour. Directly fixing the cells inside an eppendorf or on a 96-well plate is not recommended, as fixed organisms tend to adhere to the surface and will make the retrieval of fixed samples difficult.

Transmission Electron Microscopy

Spirostomum ambiguum were fixed in 2% glutaraldehyde with 4% paraformaldehyde in 1X PHEM buffer[67] for at least one hour at room temperature. The samples were stained with Safranin-O and stabilized in 1% low melting point agarose, then cut into 1mm cubes. Samples were rinsed (3×; 10 min, room temperature (RT)) in 1X PBS, and immersed in 1% osmium tetroxide with 1.6% potassium ferricyanide in 1xPBS, pH 7.4 for 1 hour. Samples were rinsed (3×; 10 min, RT) in buffer and then briefly in distilled water. Samples were then subjected to an ascending acetone gradient (10min; 35%, 50%, 70%, 80%, 90%) followed by pure acetone (2×; 10 min, RT). Samples were progressively infiltrated with Epon resin (EMS, Hatfield, PA, USA), while rocking, and then polymerized at 60℃ for 24-48 hours in silicon molds. Thick sections (200 nm) were cut using a Leica UC6 ultramicrotome (Leica, Wetzlar, Germany), collected on glass slides and used for general orientation. Thin sections (70-80 nm) were collected onto formvar-coated 50 mesh copper grids. Thin sections were post-stained with 2% aqueous uranyl acetate and Reynold's lead citrate, 5 mins each. Then sections were either imaged using a Tecnai 12 120kV TEM (FEI, Hillsboro, OR, USA) and data recorded using an UltraScan 1000 with Digital Micrograph 3 software (Gatan Inc., Pleasanton, CA, USA) at UC Berkeley, or imaged in the JEOL JEM-1400 120kV with photo taken using a Gatan Orius 2k X 2k digital camera at Stanford University. The montage image was created by SerialEM. All segmentation of organelles was done manually on Fiji.

Confocal Imaging

Spirostomum ambiguum were stained alive in 625ng/mL DiOC6(3) (Sigma-Aldrich catalog #318426-250MG) and 500nM MitoTracker™ Orange CMTMRos (Thermo Fisher Scientific catalog #M7510) for 30 minutes, followed by washing steps in 1X Carter's media.[68] The cells are then fixed in Bouin's solution for 30 minutes, and washed in 1X Carter's media until the supernatant becomes completely transparent and without any yellow-tinged color. The fixed samples are then stained with Hoechst 33342 (Invitrogen catalog #H3579) in 1:1000 dilution for 15 minutes, followed by washing steps in 1X Carter's media. The fixed samples are transferred to glass slide, mounted in Vectashield antifade mounting media (Vector labs catalog #H-1000) and sealed with #1.5 coverslip. All Chemicals are diluted from stock solution using 1X Carter's media.

We used Bouin's solution as our fixatives because of its better preservation of soft and delicate structures.[69] However, as the picric acid is a strong oxidizer and may impact the fluorophores, we used a much shorter fixation time, and all the imaging was done within 24 hours after the fixation. The confocal imaging was done on an inverted Zeiss LSM 780 multiphoton laser scanning confocal microscope, using PLAN APO 63X oil objective (NA 1.4).

Model description

In the entangled hard particle model, the cell is simplified into a two-dimensional square, the vacuoles in the cytoplasm are simplified into hard particles, and the RER is simplified into nearly in-extensible strings with zero bending energy. The total number of hard particles and strings are N_c and N_f, respectively. Each string is discretized into N_p points (and thus $(N_\mathrm{p} - 1)$ segments), and the natural length of each segment is l_0. The total length of the string is thus $l_\mathrm{f} = (N_\mathrm{p} - 1)l_0$. The first and last discretized points of each string is attached to the surface of 2 hard particles and is fixed relatively to the attached particles. There is no energy penalty associated with the changes in the exit angle between the string segment

and the surface of the particle. The forces exerted on the first or last segment of each string will be felt by the attached particles, which can cause translation and rotation. To initialize the system, the center location of the particles are randomly initialized within the square box according to a standard algorithm based on polygon partitioning. A Delaunay triangulation map is then generated based on the center location of the particles to find the neighbors,[70] with total number of edges in the Delaunay triangulation map N_{D}. The strings are initialized by randomly connecting the neighbors in the Delaunay triangulation map at opposite position, without replacement, so the same two particles will not be connected by more than one string. The phase angle of its attachment on one end, θ_1, is randomly initialized between 0 and 2π, and the phase angle of the other end is always initialized at $\theta_1 + \pi$. The degree of connectivity or topological constraint can be characterized by the filament fraction ϕ_{f}, which is defined as $\phi_{\mathrm{f}} := N_{\mathrm{f}}/N_{\mathrm{D}}$.

The position of the m-th particle is $\vec{x}_m$, and its radius is r_m. The sizes of the hard particles have a bidispersity of 1.4, with an exact 50%/50% ratio.[71] Therefore, the radius of each particle m can either be R_{c} or $1.4R_{\mathrm{c}}$, with R_{c} as the baseline radius defined for scaling of other length scale in the system. The cell in its neutral shape is a square box with side length of $L_{\mathrm{side}} = 30R_c$. The volume fraction of the system ϕ can be easily computed as $\phi = \frac{N_{\mathrm{c}}/2(\pi R_{\mathrm{c}}^2+\pi(1.4R_{\mathrm{c}})^2)}{(30R_{\mathrm{c}})^2} \approx 0.005166N_{\mathrm{c}}$. The natural length of each string is $1.4 \times 6.4 \times R_{\mathrm{c}}$. The number 6.4 is chosen such that it is slightly larger than 2π, and thus each string can wrap around 2 large particles without extension, with attached position in the opposite side (e.g., one end at the 3 o'clock position of the first particle and the other end at the 9 o'clock position of the second particle) to mimic the topology observed under TEM. The natural length of each string is a tune-able parameter, but the inequality $l_{\mathrm{f}} > \sqrt{\frac{((30R_{\mathrm{c}})^2)}{N_{\mathrm{c}}}}$ must hold to ensure that the colloidal particles are not constricted into a smaller subspace of the entire cell. The position of the i-th discretization point of the n-th string is $\vec{x}_{n,i}$, and the length of the i-th segment of the discretized string is $l_{n,i} := |\vec{x}_{n,i+1} - \vec{x}_{n,i}|$. The discretization points of the string have no size. The perpendicular distance between the center of the m-th particle

to the n-th boundary segment is $d_{m,n}$, and a function $f(\vec{x}_m)$ is used to characterize whether the center of a particle is within the boundary box. If the center of the particle is within the boundary, $f(\vec{x}_m) = 0$, while $f(\vec{x}_m) = 1$ if otherwise.

The system evolves according to an over-damped molecular dynamic scheme,[5] and the energy of the system U is composed of 4 components (Fig 3B): (1) the elastic energy in stretching the in-extensible strings U_{l}, with spring constant per vertex k_{l}, (2) the repulsive energy among particles U_{r}, with strength of repulsive interaction k_{r}, (3) the repulsive energy between particles and strings U_{rl}, (4) and the repulsive energy between particles and the boundaries U_{rb}, with strength of repulsive interaction $k_{\mathrm{rb}}k_{\mathrm{r}}$. Note that we did not include the repulsive energy of strings crossing over each other because this is a 2D approximate of the 3D RER wrapping, and the cross-sections can cross over each other with zero energy penalty because they are within the same 3D contiguous membrane. We also did not include the repulsive energy when the string hits the boundary because the system can easily relax that energy into bending of the string and create no real consequences. The particles have no Brownian motion, as we have never observed significant Brownian motion of the vacuoles in the cytoplasm.

The explicit formula of the 4 energy terms are shown as followed:[44]

$$
\begin{aligned}
U &= U_{\mathrm{l}} + U_{\mathrm{r}} + U_{\mathrm{rl}} + U_{\mathrm{rb}} \\
U_{\mathrm{l}} &= \frac{k_{\mathrm{l}} N_{\mathrm{p}}}{2} \sum_{m=1}^{N_{\mathrm{f}}} \sum_{i=1}^{N_{\mathrm{p}}-1} (l_{m,i} - l_0)^2 \\
U_{\mathrm{r}} &= \frac{k_{\mathrm{r}}}{2} \sum_{m=1}^{N_{\mathrm{c}}} \sum_{n>m}^{N_{\mathrm{c}}} (r_n + r_m - |\vec{x}_m - \vec{x}_n|)^2 \times \Theta(r_n + r_m - |\vec{v}_m - \vec{v}_n|) \\
U_{\mathrm{rl}} &= \frac{k_{\mathrm{r}}}{2} \sum_{m=1}^{N_{\mathrm{c}}} \sum_{n=1}^{N_{\mathrm{f}}} \sum_{i=1}^{N_{\mathrm{p}}} (r_m - |\vec{x}_m - \vec{x}_{n,i}|)^2 \times \Theta(r_m - |\vec{x}_m - \vec{x}_{n,i}|) \\
U_{\mathrm{rb}} &= \frac{k_{\mathrm{rb}} k_{\mathrm{r}}}{2} \sum_{m=1}^{N_{\mathrm{c}}} \sum_{n=1}^{N_{\mathrm{wall}}} (r_m - (-1)^{f(\vec{x}_m)} d_{m,n})^2 \times \Theta(r_m - (-1)^{f(\vec{x}_m)} d_{m,n})
\end{aligned}
\tag{1}
$$

The gradient of the potential energy generates forces $\vec{F}$ on the particles and the discretization

points of the strings, and can also generate torques $\vec{L}$ on the particles. With η as the viscosity, the velocity of the m-th particle is computed as $\vec{v}_m = \sum \vec{F}_m/(6\pi\eta r_m)$, and the angular velocity of the m-th particle is computed as $\vec{\omega}_m = \sum \vec{L}_m/(8\pi\eta r_m^3)$. The velocity of the discretization points of the string is computed as $\vec{v}_{n,i} = \sum \vec{F}_{n,i}/(6\pi\eta l_0)$. For our simulation, we picked $R_\mathrm{c} = 1$, and we chose both $k_\mathrm{r} = 1$ and $\eta = 1$ to make the characteristic velocity v_char of the particle to be 1. We chose k_l such that the dimensionless number $(k_\mathrm{l} l_\mathrm{f})/(6\pi\eta R_\mathrm{c} v_\mathrm{char}) = 10$, to make the strings effectively in-extensible. We chose $k_\mathrm{rb} = 1$ to make the repulsive forces from the boundary the same as from particles. Please note that the boundary is just an energy barrier, and thus particles slightly protruding out from the boundaries are expected and indicative the presence of reactive forces on boundaries.

After initialization, the system first undergoes an initial relaxation period until the kinetic energy per particle satisfies $K/N_\mathrm{c} < 10^{-10}$ and the potential energy from particles and boundaries $(U_\mathrm{r} + U_\mathrm{rb})$ per particles satisfies $(U_\mathrm{r} + U_\mathrm{rb})/N_\mathrm{c} < 10^{-8}$, or when the energy fail to change more than 1% after more than 50 iterations of relaxation to avoid an infinite while loop in the program. We use only the potential energy from particles and boundaries to determine the relaxation because U_l and U_rl will scale with the number of strings, and systems with the same volume fraction of particles yet with varying filament fractions may not be relaxed to the same degree before they start if we also include those terms. A new Delaunay triangulation diagram is computed again at the end of the initial relaxation period, which serves as a comparison for the changes in neighboring relationship among particles. After the initial relaxation period, the cell undergoes a 50% contraction in x-direction (with extension in y-direction to conserve volume), a brief hold in fully contracted state, followed by a slow relaxation in x-direction to return to its original shape and a brief hold in fully relaxed state, in a scheme similar to the contraction process of *Spirostomum ambiguum*.[4] In the contraction phase, a constant boundary force F is imposed, and the reactive forces of the system on the side walls F_x is computed. The bounding box is then shrunken by $(F - F_x)/(6\pi\eta L_\mathrm{side})$. The size of the bounding box is adjusted every 200 simulation time unit, and the process repeated

until 50% contraction in x-direction was achieved. The relaxation process is discretized into 100 steps, with the bounding box shape adjusted every 2000 simulation time unit. The relaxation phase is rather arbitrarily set as our focus of analysis is mainly on contraction kinematics, and the majority of energy dissipation is determined by the contraction phase. The contact number among the particles, the changes in the Delaunay diagram, potential energy and the forces on the boundaries are recorded and used for the plot. The code is written in Python3 and the systems of ODEs are solved by the backward differentiation formula (BDF) method[72] of the package odespy.[73]

Several limitation exists for the model we used. First of all, we used a hard particles instead of a deformable soft particles in our system. This is because the topological constraints we observed is suggesting a more general mechanism to introduce braking function and structural stabilization. Also, the jamming physics of geometrically constrained hard particles itself is already an under-explored topic. Secondly, the length of the strings is set to be uniform, while in reality, we would expect the length of bridging ER should have some distribution, even though we do not think this will change the main conclusions of the model. Finally, several key features of the contraction process of *Spirostomum* are not accounted, these include the asymmetry of the contraction process,[74] and the torsional component of the contraction process.[75] While we expect the asymmetry should do little with respect to the braking of cytoplasm, it is possible for the torsional component to bring the system under topological confinement faster than pure contraction. However, as it is not possible to introduce torsion in a 2D simulation, we will leave that as future work.

As there are no previous studies on this topic that can provide a suitable validation case, we validate our code by monitoring the volume fraction of jamming transition using a different simulation protocol but the same code base as above (Supplementary Figure S3). In this simulation, we implement a system with periodic boundary condition and no strings attached to the hard particles. We initialize the system with a volume fraction way-below jamming transition (50%∼65%) and gradually shrink the box with a step size

of 0.5% and minimize the total potential energy. The jamming transition was identified as the point when $(U_{\mathrm{r}} + U_{\mathrm{rb}})/N_{\mathrm{c}}$ fail to relax below 10^{-8}, or the jump in potential energy (see Supplementary Figure S3). The volume fraction of jamming transition identified by our code base is consistent with previously reported number.[71] The code is available on Github (https://github.com/jrchang612/Entangled_Hard_Particles).

Details on tracing neighboring relationship

In our analysis of the preservation of neighboring relationship, we used edges in Delaunay diagram to trace the neighbor. However, as the particles are confined in a square boundary, there are often spurious neighboring connections found in Delaunay diagram that should not be considered as a true neighbor. To eliminate that, if the distance between the center of two "neighboring" particles is greater than $4 \times 1.4R_{\mathrm{c}}$, that neighboring relationship is considered spurious and eliminated from further analysis (Supplementary Figure S4).

Table-top experiments

To create the macroscopic counterpart of the entangled RER-vacuolar system, we used table tennis balls (KEVENZ, diameter 1.57 inch, as international standard) wrapped by sheer fabric backdrop curtains (Anteer, Crystal Organza Tulle Sheer Fabric Backdrop Curtains for Wedding Baby Shower Birthday Party Event Decor, of size 18.5 in $\times$ 23 in, with thickness of 0.12 mm). In the topologically constrained group, the fabric was cut into interconnected stripes of roughly 2 cm thick. 45 table tennis balls were randomly attached to stripes in an interwoven fashion, and each table tennis balls were connected to 2 stripes, using super glue and protected by tapes. In the control group, the fabric was joined to form a bag, and 45 table tennis balls were put into the bag. We also applied two stripes of tapes on each table tennis ball in the control group, as the presence of tape can increase the friction among balls. The bag was sealed afterwards. We chose the control group to have the same amount of material, rather than control based on other parameters (such as control to be of the same

convex hall) because it is closer to a biological scenario – an organism has a roughly fixed amount of resources or energy to make the same amount of RER and vacuoles, and their task is to arrange the material topologically to optimize its physical properties.

To test the ability to resist external load in two groups, the curtain in the control group was folded into the pile of table tennis ball to make a comparable height as the topologically constrained group. The samples were used for video shooting and compression testing. In the videos, two objects with different shape and weight – a giant ruler (weight 375gm, bottom surface dimension 24 in $\times$ 2 in), and a book (weight 2450gm, bottom surface dimension 11.13 in $\times$ 8.63 in) were tested. The object was released right above the samples and the video was recorded using smart phone.

Compression testing was done on Tensiometer Instron 5565, with compression plate of diameter 150mm installed and a 5kN load cell. The height of the samples was adjusted to 135mm, and a simple compression test at a compression rate of 50mm/min with no preload was performed. The test was terminated when the displacement becomes greater than 110mm or when force becomes greater than 5kN. As the compression testing inevitably destroy the sample, the compression testing was done after the video shooting and 3 different samples were used in each group for triplicate. In addition to the compression testing on entangled and untangled samples, we also did compression testing on individual table tennis balls (simple compression test, compression rate 50mm/min, no preload, test terminates when displacement $>$ 35mm or force $>$ 5kN) and extension testing on 2cm-thick fabric stripes (simple extension test with preload, extension rate 50mm/min, test terminates when force drop $>$ 40% for force $>$ 1kN). The reactive forces of the entangled and untangled samples were normalized by the reactive forces of individual table tennis ball when it is compressed by 5mm, because that corresponds to a visually indisputable deformation. The peak extension force of the 2cm fabric stripes is 37.2 $\pm$ 1.9N (mean $\pm$ standard error), and the reactive forces of individual table tennis ball when it is compressed by 5mm is 152.1 $\pm$ 0.7 N (mean $\pm$ standard error).

Acknowledgement

We thank all members of the Prakash Lab for scientific discussions and comments, including Arnold JTM Mathijssen, Hongquan Li, Deepak Krishnamurthy, Eliott Flaum and Samhita Banvar. We thank Rebecca Konte, Rahul Chajwa and Junqin Zhu for figure graphics and video. We thank Dr. Danielle Jorgens and Reena Zalpuri at the University of California Berkeley Electron Microscope facility service for advice and assistance in electron microscopy and staff of Stanford Cell Sciences Imaging Facility (ARRA Award Number 1S10RR026780-01), Stanford Nano Shared Facilities (NSF award ECCS-2026822). We thank Professor Corey S. O'Hern and Jack Treado for helpful discussion on modeling particle system. We thank Deepak Krishnamurthy for providing his object-oriented code base, and we thank Professor Paul Nuyujukian for providing the singularity container. RC gratefully acknowledge support by Stanford University Bio-X SIGF Fellows Program and by the Ministry of Education in Taiwan. This work was support by HHMI Faculty Fellows Award (M.P), BioHub Investigator Fellowship (M.P), Keck Foundation Research Grant, and NSF CCC (DBI1548297).

References

(1) Nüchter, T.; Benoit, M.; Engel, U.; Özbek, S.; Holstein, Nanosecond-scale kinetics of nematocyst discharge. *Current Biology* **2006**, *16*, R316–R318.

(2) Hawkes, R. B.; Holberton, D. V. Myonemal contraction of Spirostomum I. Kinetics of contraction and relaxation. *Journal of Cellular Physiology* **1974**, *84*, 225–236.

(3) Weis-Fogh, T.; Amos, W. B. Evidence for a new mechanism of cell motility. *Nature* **1972**, *236*, 301–304.

(4) Mathijssen, A. J.; Culver, J.; Bhamla, M. S.; Prakash, M. Collective intercellular communication through ultra-fast hydrodynamic trigger waves. *Nature* **2019**, *571*, 560–564.

(5) Gao, G. J.; Bławzdziewicz, J.; O'Hern, C. S. Frequency distribution of mechanically stable disk packings. *Physical Review E - Statistical, Nonlinear, and Soft Matter Physics* **2006**, *74*, 061304.

(6) Van Hecke, M. Jamming of soft particles: geometry, mechanics, scaling and isostaticity. *Journal of Physics: Condensed Matter* **2009**, *22*, 033101.

(7) Wilson, A. M.; Lowe, J. C.; Roskilly, K.; Hudson, P. E.; Golabek, K. A.; McNutt, J. W. Locomotion dynamics of hunting in wild cheetahs. *Nature* **2013**, *498*, 185–189.

(8) Yaraghi, N. A.; Trikanad, A. A.; Restrepo, D.; Huang, W.; Rivera, J.; Herrera, S.; Zhernenkov, M.; Parkinson, D. Y.; Caldwell, R. L.; Zavattieri, P. D. et al. The Stomatopod Telson: Convergent Evolution in the Development of a Biological Shield. *Advanced Functional Materials* **2019**, *29*, 1902238.

(9) Ha, N. S.; Lu, G.; Shu, D. W.; Yu, T. X. Mechanical properties and energy absorption characteristics of tropical fruit durian (Durio zibethinus). *Journal of the Mechanical Behavior of Biomedical Materials* **2020**, *104*, 103603.

(10) Ferenczi, M. A.; Bershitsky, S. Y.; Koubassova, N. A.; Kopylova, G. V.; Fernandez, M.; Narayanan, T.; Tsaturyan, A. K. Why muscle is an efficient shock absorber. *PLoS ONE* **2014**, *9*, e85739.

(11) Roberts, T. J.; Konow, N. How tendons buffer energy dissipation by muscle. *Exercise and Sport Sciences Reviews* **2013**, *41*, 186–193.

(12) Li, T. T.; Wang, H.; Huang, S. Y.; Lou, C. W.; Lin, J. H. Bioinspired foam composites resembling pomelo peel: Structural design and compressive, bursting and cushioning properties. *Composites Part B: Engineering* **2019**, *172*, 290–298.

(13) Stein, F. *Der Organismus der Infusionsthiere nach eigenen Forschungen in system-*

atischer Reihenfolge bearb. von Friedrich Stein.; W. Engelmann,: Leipzig,, 1867; pp 187–207.

(14) Hawkes, R. B.; Holberton, D. V. Myonemal contraction of spirostomum. II. Some mechanical properties of the contractile apparatus. *Journal of Cellular Physiology* **1975**, *85*, 595–602.

(15) Yao, M.; Goult, B. T.; Klapholz, B.; Hu, X.; Toseland, C. P.; Guo, Y.; Cong, P.; Sheetz, M. P.; Yan, J. The mechanical response of talin. *Nature Communications* **2016**, *7*, 11966.

(16) Abraham, V.; Krishnamurthi, V.; Taylor, D.; Lanni, F. The actin-based nanomachine at the leading edge of migrating cells. *Biophysical journal* **1999**, *77*, 1721–1732.

(17) Upadhyaya, A.; Sheetz, M. P. Tension in Tubulovesicular Networks of Golgi and Endoplasmic Reticulum Membranes. *Biophysical Journal* **2004**, *86*, 2923–2928.

(18) Gogia, S.; Neelamegham, S. Role of fluid shear stress in regulating VWF structure, function and related blood disorders. 2015; `https://pubmed.ncbi.nlm.nih.gov/26600266/`.

(19) Bishop, A. Memoirs: Some Observations Upon Spirostomum ambiguum (Ehrenberg). *Journal of Cell Science* **1923**, *s2-67*, 391–434.

(20) Hammond, J. C. A microdissection study of the protoplasm of vacuolated spirostomum. *Zeitschrift für Zellforschung und Mikroskopische Anatomie* **1937**, *25*, 776–786.

(21) Bary, B. M. Studies on the Freshwater Ciliates of New Zealand Part I A General Morphology of Bursaria Truncatella Muller. *Transactions and Proceedings of the Royal Society of New Zealand* **1950**, *78*, 301–310.

(22) Foissner, W.; Berger, H. *A user-friendly guide to the ciliates (Protozoa, Ciliophora)*

commonly used by hydrobiologists as bioindicators in rivers, lakes, and waste waters, with notes on their ecology; 1991; Vol. 35; p 375482.

(23) Raven, J. A. The Vacuole: a Cost-Benefit Analysis. *Advances in Botanical Research* **1997**, *25*, 59–86.

(24) Wichterman, R.; Figge, F. H. J. Lethality and the biological effects of X-rays in Paramecium: radiation resistance and its variability. *The Biological Bulletin* **1954**, *106*, 253–263.

(25) Laporte, C.; Kosta, A.; Klein, G.; Aubry, L.; Lam, D.; Tresse, E.; Luciani, M. F.; Golstein, P. A necrotic cell death model in a protist. *Cell Death & Differentiation 2007 14:2* **2006**, *14*, 266–274.

(26) Shubin, A.; Demidyuk, I.; Komissarov, A.; Rafieva, L.; Kostrov, S. Cytoplasmic vacuolization in cell death and survival. *Oncotarget* **2016**, *7*, 55863–55889.

(27) Yamanaka, T.; Nukina, N. ER Dynamics and Derangement in Neurological Diseases. *Frontiers in Neuroscience* **2018**, *12*, 91.

(28) English, A. R.; Voeltz, G. K. Endoplasmic Reticulum Structure and Interconnections with Other Organelles. *Cold Spring Harbor Perspectives in Biology* **2013**, *5*, a013227.

(29) Scorrano, L.; De Matteis, M. A.; Emr, S.; Giordano, F.; Hajnóczky, G.; Kornmann, B.; Lackner, L. L.; Levine, T. P.; Pellegrini, L.; Reinisch, K. et al. Coming together to define membrane contact sites. *Nature Communications 2019 10:1* **2019**, *10*, 1–11.

(30) Helle, S. C.; Kanfer, G.; Kolar, K.; Lang, A.; Michel, A. H.; Kornmann, B. Organization and function of membrane contact sites. *Biochimica et Biophysica Acta (BBA) - Molecular Cell Research* **2013**, *1833*, 2526–2541.

(31) Browne, K. M. X.—The Golgi apparatus and other cytoplasmic bodies in Spirostomum ambiguum. *Journal of the Royal Microscopical Society* **1938**, *58*, 188–199.

(32) Moore, J. E. S. On the Structural Differentiation of the Protozoa as seen in Microscopic Sections. *Zoological Journal of the Linnean Society* **1893**, *24*, 364–368.

(33) Ramoino, P.; Diaspro, A.; Fato, M.; Beltrame, F.; Robello, M. Changes in the endoplasmic reticulum structure of Paramecium primaurelia in relation to different cellular physiological states. *Journal of Photochemistry and Photobiology B: Biology* **2000**, *54*, 35–42.

(34) Gravish, N.; Franklin, S. V.; Hu, D. L.; Goldman, D. I. Entangled Granular Media. *Physical Review Letters* **2012**, *108*, 208001.

(35) Mlot, N. J.; Tovey, C. A.; Hu, D. L. Fire ants self-assemble into waterproof rafts to survive floods. *Proceedings of the National Academy of Sciences* **2011**, *108*, 7669–7673.

(36) Phonekeo, S.; Mlot, N.; Monaenkova, D.; Hu, D. L.; Tovey, C. Fire ants perpetually rebuild sinking towers. *Royal Society Open Science* **2017**, *4*.

(37) Panagiotou, E.; Millett, K. C.; Atzberger, P. J. Topological Methods for Polymeric Materials: Characterizing the Relationship Between Polymer Entanglement and Viscoelasticity. *Polymers 2019, Vol. 11, Page 437* **2019**, *11*, 437.

(38) Parisi, D.; Costanzo, S.; Jeong, Y.; Ahn, J.; Chang, T.; Vlassopoulos, D.; Halverson, J. D.; Kremer, K.; Ge, T.; Rubinstein, M. et al. Nonlinear Shear Rheology of Entangled Polymer Rings. *Macromolecules* **2021**, *54*, 2811–2827.

(39) Aejmelaeus-Lindström, P.; Willmann, J.; Tibbits, S.; Gramazio, F.; Kohler, M. Jammed architectural structures: Towards large-scale reversible construction. *Granular Matter* **2016**, *18*, 1–12.

(40) Iliev, P. S.; Wittel, F. K.; Herrmann, H. J. Inversion of force lines in fiber-reinforced jammed granular material. *The European Physical Journal E 2021 44:4* **2021**, *44*, 1–6.

(41) White, B. C.; Garland, A.; Alberdi, R.; Boyce, B. L. Interpenetrating lattices with enhanced mechanical functionality. *Additive Manufacturing* **2021**, *38*, 101741.

(42) Shivers, J. L.; Feng, J.; van Oosten, A. S. G.; Levine, H.; Janmey, P. A.; MacKintosh, F. C. Compression stiffening of fibrous networks with stiff inclusions. *Proceedings of the National Academy of Sciences* **2020**, *117*, 21037–21044.

(43) Zhang, J.; Majmudar, T. S.; Sperl, M.; Behringer, R. P. Jamming for a 2D granular material. *Soft Matter* **2010**, *6*, 2982–2991.

(44) Boromand, A.; Signoriello, A.; Ye, F.; O'Hern, C. S.; Shattuck, M. D. Jamming of Deformable Polygons. *Physical Review Letters* **2018**, *121*, 248003.

(45) Zamponi, N.; Zamponi, E.; Cannas, S. A.; Billoni, O. V.; Helguera, P. R.; Chialvo, D. R. Mitochondrial network complexity emerges from fission/fusion dynamics. *Scientific Reports 2017 8:1* **2018**, *8*, 1–10.

(46) Wu, Y.; Whiteus, C.; Xu, C. S.; Hayworth, K. J.; Weinberg, R. J.; Hess, H. F.; De Camilli, P. Contacts between the endoplasmic reticulum and other membranes in neurons. *Proceedings of the National Academy of Sciences of the United States of America* **2017**, *114*, E4859–E4867.

(47) Cates, M. E.; Wittmer, J. P.; Bouchaud, J. P.; Claudin, P. Jamming, Force Chains, and Fragile Matter. *Physical Review Letters* **1998**, *81*, 1841.

(48) Ambrosini, A.; Rayer, M.; Monier, B.; Suzanne, M. Mechanical Function of the Nucleus in Force Generation during Epithelial Morphogenesis. *Developmental Cell* **2019**, *50*, 197–211.e5.

(49) Petrie, R.; Koo, H.; Yamada, K. Generation of compartmentalized pressure by a nuclear piston governs cell motility in a 3D matrix. *Science (New York, N.Y.)* **2014**, *345*, 1062–1065.

(50) Lee, H. P.; Alisafaei, F.; Adebawale, K.; Chang, J.; Shenoy, V. B.; Chaudhuri, O. The nuclear piston activates mechanosensitive ion channels to generate cell migration paths in confining microenvironments. *Science Advances* **2021**, *7*.

(51) Hagihara, T.; Toyota, M. Mechanical Signaling in the Sensitive Plant Mimosa pudica L. *Plants 2020, Vol. 9, Page 587* **2020**, *9*, 587.

(52) Merta, H.; Carrasquillo Rodríguez, J. W.; Anjur-Dietrich, M. I.; Vitale, T.; Granade, M. E.; Harris, T. E.; Needleman, D. J.; Bahmanyar, S. Cell cycle regulation of ER membrane biogenesis protects against chromosome missegregation. *Developmental cell* **2021**,

(53) Schwarz, D. S.; Blower, M. D. The endoplasmic reticulum: Structure, function and response to cellular signaling. *Cellular and Molecular Life Sciences* **2016**, *73*, 79–94.

(54) Liu, A. J.; Nagel, S. R. Jamming is not just cool any more. *Nature 1998 396:6706* **1998**, *396*, 21–22.

(55) Qiao, P.; Yang, M.; Bobaru, F. Impact Mechanics and High-Energy Absorbing Materials: Review. *Journal of Aerospace Engineering* **2008**, *21*, 235–248.

(56) Zorzetto, L.; Ruffoni, D. Wood-Inspired 3D-Printed Helical Composites with Tunable and Enhanced Mechanical Performance. *Advanced Functional Materials* **2019**, *29*, 1805888.

(57) Zou, M.; Xu, S.; Wei, C.; Wang, H.; Liu, Z. A bionic method for the crashworthiness design of thin-walled structures inspired by bamboo. *Thin-Walled Structures* **2016**, *101*, 222–230.

(58) Ruan, D.; Lu, G.; Wang, B.; Yu, T. X. In-plane dynamic crushing of honeycombs - A finite element study. *International Journal of Impact Engineering* **2003**, *28*, 161–182.

(59) Rajak, D. K.; Kumaraswamidhas, L.; Das, S. An Energy Absorption Behaviour of Foam Filled Structures. *Procedia Materials Science* **2014**, *5*, 164–172.

(60) Rivera, J.; Hosseini, M. S.; Restrepo, D.; Murata, S.; Vasile, D.; Parkinson, D. Y.; Barnard, H. S.; Arakaki, A.; Zavattieri, P.; Kisailus, D. Toughening mechanisms of the elytra of the diabolical ironclad beetle. *Nature* **2020**, *586*, 543–548.

(61) Zhang, J.; Lu, G.; You, Z. Large deformation and energy absorption of additively manufactured auxetic materials and structures: A review. *Composites Part B: Engineering* **2020**, *201*, 108340.

(62) Lehman, W. J.; Rebhun, L. I. The structural elements responsible for contraction in the ciliate Spirostomum. *Protoplasma* **1971**, *72*, 153–178.

(63) Ishida, H.; Shigenaka, Y.; Imada, M. Fibrillar System and Possible Control Mechanism for the Cycle of Contraction and Elongation of Spirostomum ambiguum : Cell Biology. *Zoological Science* **1988**, *5*, 973–978.

(64) Ishida, H.; Shigenaka, Y. Cell model contraction in the ciliatespirostomum. *Cell Motility and the Cytoskeleton* **1988**, *9*, 278–282.

(65) Arceri, F.; Corwin, E. I. Vibrational Properties of Hard and Soft Spheres Are Unified at Jamming. *Physical Review Letters* **2020**, *124*, 238002.

(66) Hummer, P. J. Culturing & Using Protozoans in the Laboratory. *American Biology Teacher* **1993**, *55*, 357–360.

(67) Schliwa, M.; Van Blerkom, J. Structural interaction of cytoskeletal components. *Journal of Cell Biology* **1981**, *90*, 222–235.

(68) Carter, L. Ionic Regulation in the Ciliate Spirostomum Ambiguum. *Journal of Experimental Biology* **1957**, *34*, 71–84.

(69) Singhal, P.; Singh, N. N.; Sreedhar, G.; Banerjee, S.; Batra, M.; Garg, A. Evaluation of Histomorphometric Changes in Tissue Architecture in Relation to Alteration in Fixation Protocol – An Invitro Study. *Journal of Clinical and Diagnostic Research : JCDR* **2016**, *10*, ZC28.

(70) Delaunay, B. Sur la sphère vide. A la mémoire de Georges Voronoï. *Bulletin de l'Académie des Sciences de l'URSS. Classe des sciences mathématiques et na* **1934**, 793–800.

(71) Koeze, D. J.; Vågberg, D.; Tjoa, B. B.; Tighe, B. P. Mapping the jamming transition of bidisperse mixtures. *EPL* **2016**, *113*, 54001.

(72) Curtiss, C. F.; Hirschfelder, J. O. Integration of Stiff Equations. *Proceedings of the National Academy of Sciences* **1952**, *38*, 235–243.

(73) Langtangen, H. P.; Wang, L. Odespy Software Package. 2015; `https://github.com/hplgit/odespy`, `https://github.com/hplgit/odespy`.

(74) Jahn, T. L. Contraction of protoplasm. II. Theory: Anodal vs. Cathodal in relation to calcium. *Journal of Cellular Physiology* **1966**, *68*, 135–148.

(75) Ishida, H.; Suzaki, T.; Shigenaka, Y. Cell body contraction of Spirostomum does not involve shortening of inter-kinetosomal distance along ciliary lines. *Zoological Science* **1996**, *13*, 669–672.

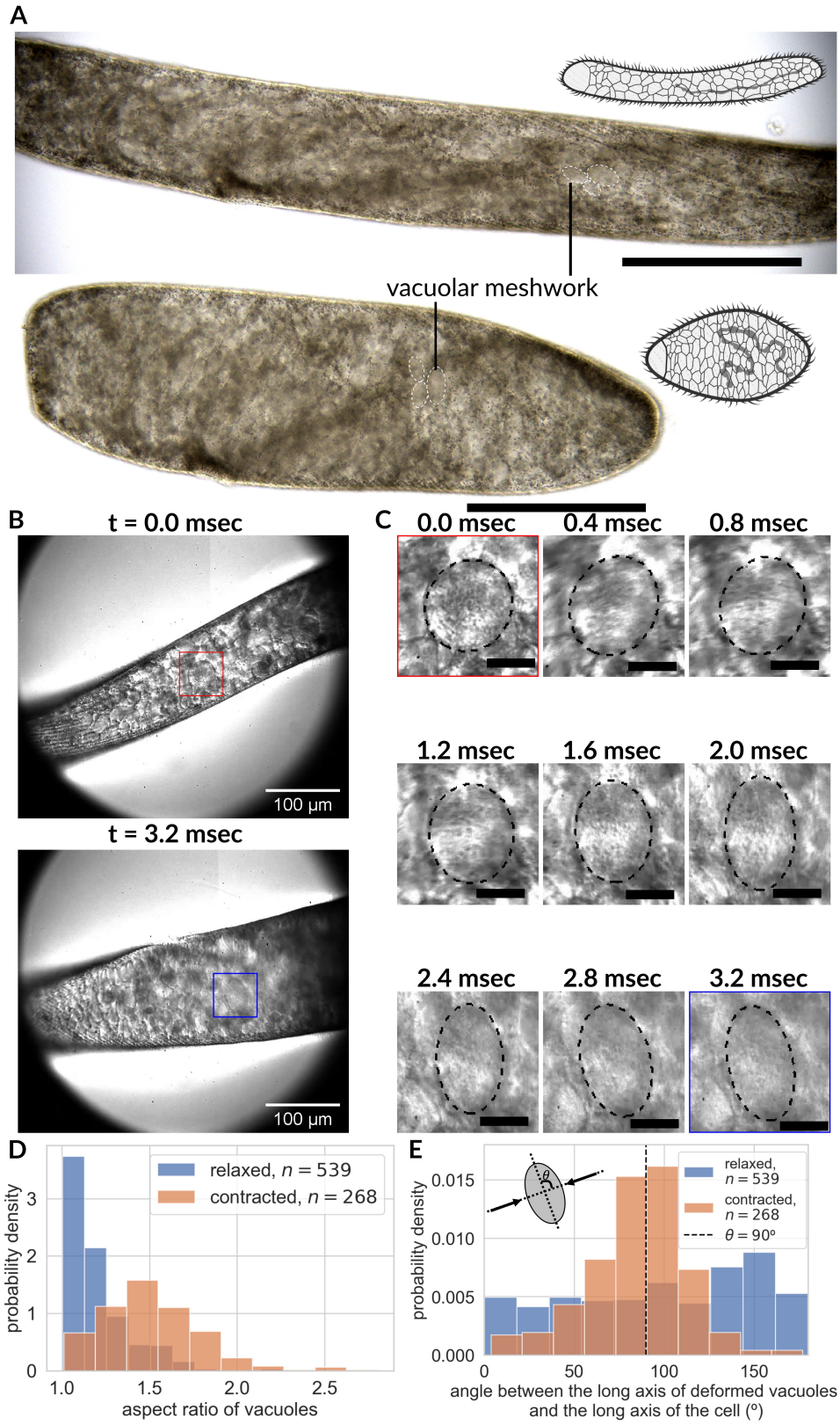

Figure 1: (Caption next page.)

Figure 1: (Previous page.) Vacuolar meshwork inside a giant cell *Spirostomum ambiguum* undergoing ultra-fast contractions, leading to organelle deformations. (A) Color differential interference contrast (DIC) images of the same *Spirostomum ambiguum* cell before and after an ultrafast contraction event, depicting ∼50% length shortening in less than 10 msec while maintaining cell volume. The cellular cytoplasm is filled with vacuoles packed at high density. Scale bar 200 μm. (B) Single cell contraction under high speed camera reveals large scale deformation (40% deformation from spherical to ellipsoidal) in vacuoles under compressive strain in first 3.2 millisecond of the contractile process. The red box marks one vacuole before contraction while blue box marks the same vacuole after a single contraction event. Image sequence of the detailed shape change under this compressive load for the same vacuole is shown in (C) at 400 microsecond time interval. Also see Supplementary Video S1&S2. Scale bar 20 μm. (D) The histogram of the aspect ratio of deforming vacuoles in relaxed and contracted organisms quantitatively establishes that the vacuoles are indeed deformed due to the ultrafast contraction process and relax back to minimum energy spherical shape at longer time scale. (G) The histogram of the angle between the long axis of the vacuoles and the long axis of the cell body before and after the contraction depicts the deformation is normal to the compressive stress. Here we define the direction of the long axis of the cell body as the x-direction, and the direction of the short axis as the y-direction.

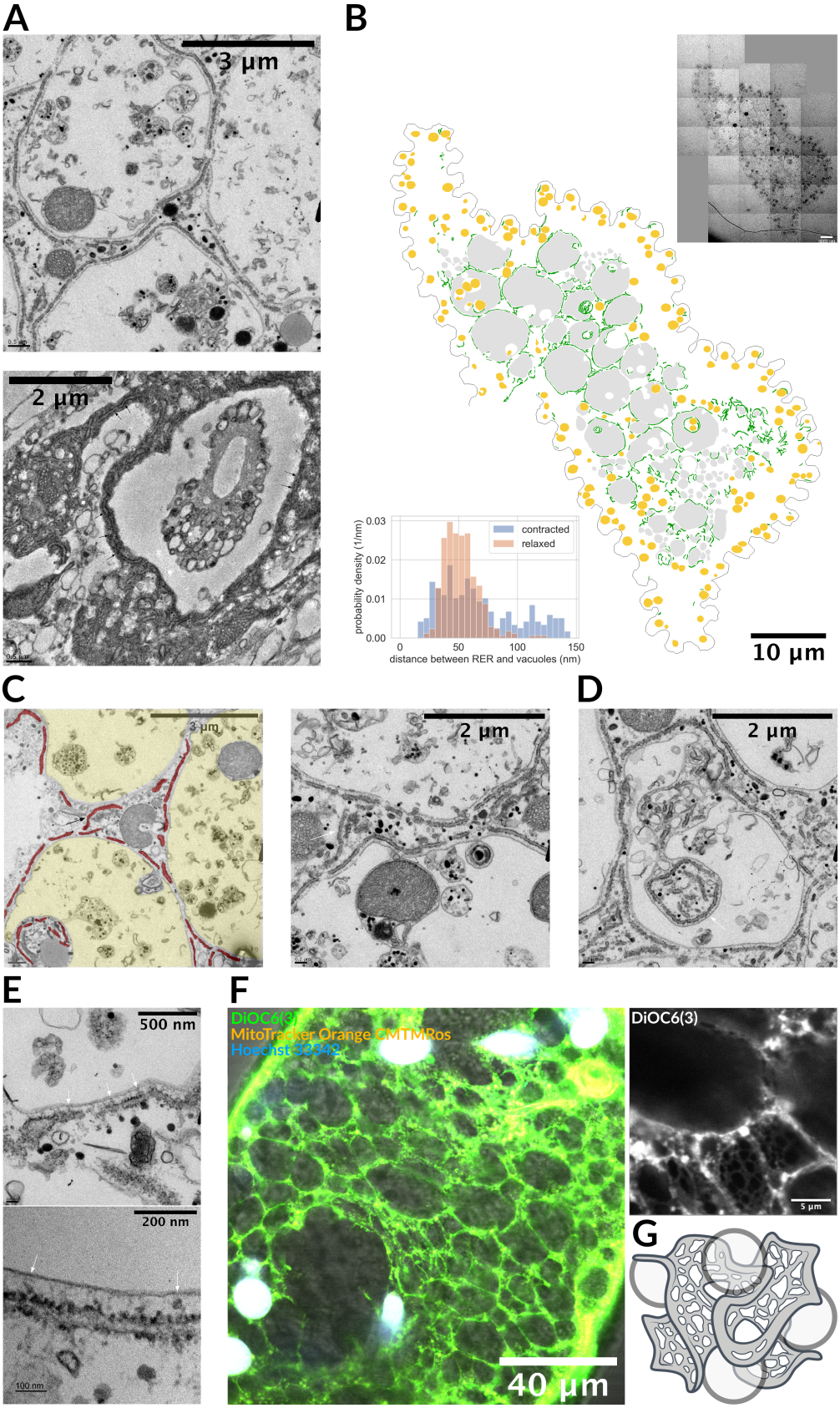

Figure 2: (Caption next page.)

Figure 2: (Previous page.) Intimate spatial relationship between endoplasmic reticulum and vacuolar meshwork. (A) High magnification of TEM imaging of *Spirostomum ambiguum* cell before (upper) and after (lower) an ultrafast contraction event shows the vacuolated cytoplasm, and the rough endoplasmic reticulum is intimately wrapping around the vacuoles in both cases. Also see Supplementary Figure S1 for low magnification of the entire cross-section. (B) Montage of the entire cross-section of a relaxed organism and its corresponding segmentation of rough endoplasmic reticulum (green), vacuoles (gray) and mitochondria (yellow). The entangled topology between RER and vacuoles spans through the entire cross section and is not limited to a certain region. The inset on the right upper corner shows the original image of the montage cross-section image. Width of the original image 65.287μm. The histogram on the lower left corner shows the distance between endoplasmic reticulum and its nearby vacuoles in contracted and relaxed organisms under TEM. In relaxed organism, the distance between endoplasmic reticulum and its nearby vacuole falls between 30 to 70 nm, while in contracted organism, this distance becomes more variable, but it still falls below 150nm. (C) TEM occasionally revealed the "bridging" endoplasmic reticulum (arrows) that connects the endoplasmic reticulum of two nearby vacuoles. The presence of such structure is expected and necessary, as endoplasmic reticulum is known to be a single continuous lumen. RER false colored in red and vacuoles false colored in yellow on the left figure. (D) We also observed extreme tram-tracking of rough endoplasmic reticulum following the contour of vacuoles even when cytoplasm invaginating inwards to the vacuoles (white arrows). (E) Under even higher magnification, we can see some materials (white arrows) between RER and nearby vacuoles that might be the protein connections between the two. (F) Confocal imaging of the endoplasmic reticulum and vacuolar meshwork of a contracted organism (left) and a cropped magnified region (upper right). The image shows a fenestrated web-like structure of endoplasmic reticulum wrapping around vacuolar meshwork throughout the entire organism. Also see Supplementary Video S3-S5 for the video of complete z-stack, and Supplementary Figure S2. (G) 3D schematic drawing of the entangled topology between fenestrated ER and vacuoles.

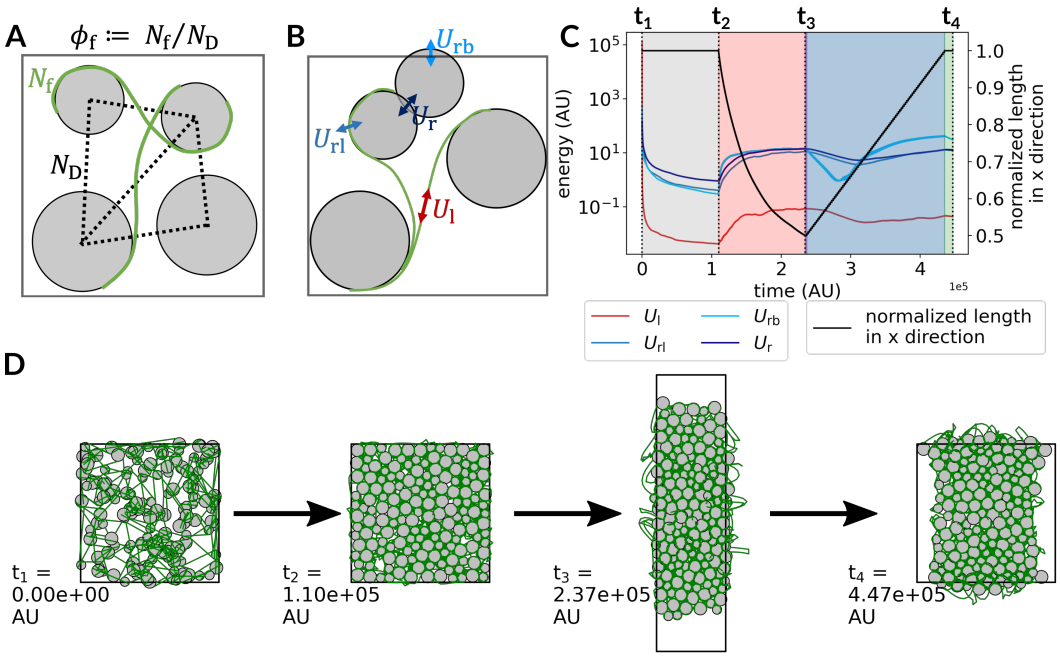

Figure 3: A 2D entangled hard particle model allows us to study the effect of topological constraints on the mechanical properties of packed vacuoles in response to a large shape changes. (A) Filament fraction, which is defined as the ratio between the number of strings (N_f) and the number of edges in the Delaunay diagram (N_D), is used to described the degree of connectivity or the degree of topological constraints in the system. Volume fraction is defined as the ratio between the total area of particles and the area enclosed by the boundary.(B) The energy terms in the model include particle-particle repulsive energy (U_r), particle-string repulsive energy (U_{rl}), particle-boundary repulsive energy (U_{rb}), and the stretching energy of strings (U_l). The system evolves according to over-damped molecular dynamic scheme. (C) & (D) The deformation schedule, the changes of energy profile, and the snapshots of of the system throughout the simulation at time point t_1-t_4. The volume fraction of the simulation is 0.83, and the bidispersity is 1.4. A constant boundary force is applied to deform the system during the contraction phase, and the volume fraction was kept constant throughout the simulation. The kinematics of the relaxation phase is artificially set, just to complete a cycle. Initially, 160 particles were randomly connected by 324 Hookean springs with zero bending modulus. After the stabilization of the initial configuration (gray), the system underwent contraction (pink) and relaxation (blue), just like the contraction process of *Spirostomum ambiguum*. Also see Supplementary Video S6-S7.

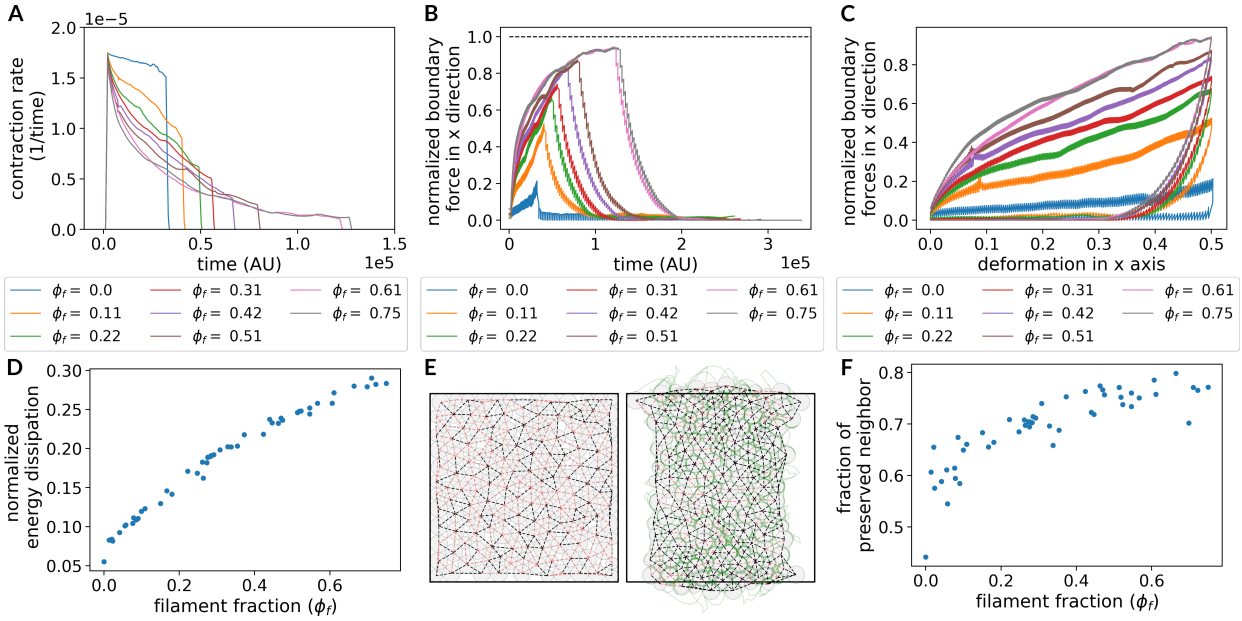

Figure 4: Geometric constraints turns an entangled particle system into a topological damper in constant force simulation. Systems with the same volume fraction of 0.83 but different filament fractions were compressed by a constant boundary force. (A) Kinematics of the contraction process. Increasing topological constraints causes a rapid drop in contraction rate, showing its role as a damper. (B) Time series changes of the boundary forces in x-direction normalized with respect to external load. Increasing topological constraints increases the ability of the system to counteract external forces, which explains the rapid slow down in contraction kinematics. The dashed horizontal line indicates the magnitude of external load, normalized to 1. (C) Boundary force in x-direction - deformation loop. The boundary forces are normalized with respect to external load. Increasing topological constraints increases the ability of the system to dissipate energy. (D) Energy dissipation, computed from the area enclosed by the curve in (C), with all 50 simulation results. (E) Increasing topological constraints helps preserve the neighboring relationship after a contraction event. The neighbors are identified as the edges on Delaunay diagram, and the list of neighboring particles are compared before and after a single cycle of contraction. New neighbors are colored in pink and preserved neighbors are colored in black. The figure on the left hand side has 0 filament fraction, and 44.2% of the neighbors are preserved. The figure on the right hand side has 70% filament fraction, and 77.1% of the neighbors are preserved. (F) The preserved neighbor of the system after a single cycle of contraction, with all 50 simulation results.

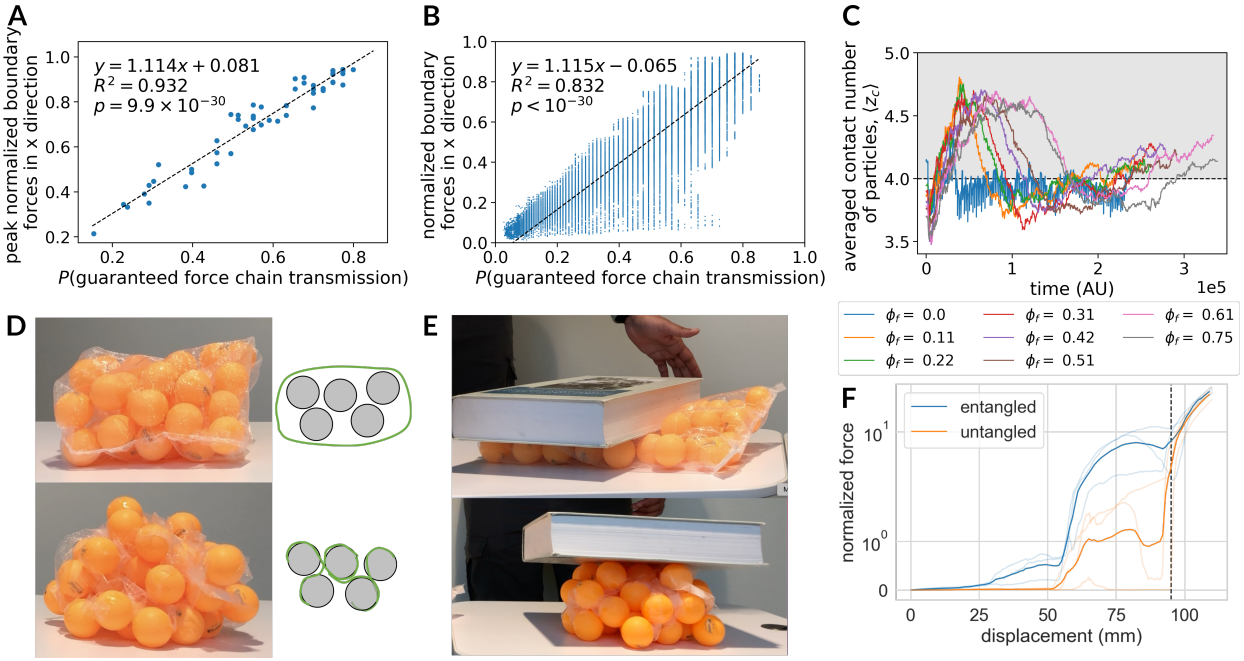

Figure 5: Phenomenon of topologically induced jamming. The strings in the system create more contact with neighboring particles, which makes the particles become overly constrained and jammed more easily. (A) By computing the probability of force chain propagation at the moment of peak contraction, we can predict the magnitude of peak reactive forces against external load. (B) If we compute the probability of force chain propagation throughout the contraction process, we can even predict the entire curve of boundary forces. Data composed of 50 simulations. Also see Supplementary Figure S5 for individual simulation time curves. (C) If we only look at the contact among particles, as is done in the literature, increasing topological constraints cause a prolonged jammed state in the system. (D)-(F) We used 45 table tennis balls and fabrics to demonstrate the concept of topological constraints induced jamming. In the two system, there are same numbers of table tennis balls and same amount of fabrics, but one (the upper one in (D)) was not arranged in an entangled topology while the other (the lower one in (D)) was (see Method for details). (E) After applying a 2450g external load, we can easily see that the entangled system had a better ability to resist external load. Also see Supplementary Video S8 & S9. (F) The differences between entangled and untangled systems are also demonstrated quantitatively in compression testing. The mean curve of the 3 samples in each group was drawn in solid line while the individual experiment data were drawn transparently. The reactive forces of the system were normalized by the reactive forces of individual table tennis ball when they are compressed by 5mm (mean $\pm$ standard error $= 152.1 \pm 0.7$ N). As the height of the samples were adjusted to 135mm initially and the height of individual table tennis ball is 40mm, a compression of 95mm (dashed vertical line) corresponds to the onset of unavoidable deformation of table tennis ball and we can see a rapid increase in reactive forces in all traces. Also see Supplementary Video S10 & S11.